

MICROSTRUCTURAL INVESTIGATION OF HARD METALS BY COMBINATION OF ELECTRON BACKSCATTER DIFFRACTION AND X-RAY DIFFRACTION

M. Dopita¹, D. Rafaja¹, D. Chmelik¹, A. Salomon¹, D. Janisch², and W. Lengauer²

¹TU Bergakademie Freiberg, Institute of Materials Science, Germany

²Vienna University of Technology, Institute for Chemical Technologies and Analytics, Austria

Keywords

XRD, EBSD, hard metals, ceramic–metal composites, WC-Co, Ti(C,N)

Abstract

A combination of the Electron Backscatter Diffraction (EBSD) and X-ray diffraction (XRD) was used for the investigation of the microstructural properties of hard metals. A set of specimens containing hex-WC and fcc-Ti(C,N) as hard phases and Co (and Ni) as a binder was prepared by varying the WC / Ti(C,N) ratio. Due to the combination of a good spatial and angular resolution, the EBSD technique yields unique information on the orientation of individual crystallites, on the grain/subgrain morphology, on the grain size distribution, on the misorientation of the grain boundaries, and on the character of the grain boundaries (GBs) distributions for each individual hard phase present in the sample. Owing to its excellent resolution in reciprocal space, the XRD revealed the distribution of the lattice parameters in the fcc hard-phase grains, from which the composition gradients in the hard phases were calculated using an appropriate microstructure model. This microstructure model was built with the aid of the results obtained from the SEM/EBSD and SEM/EDX investigations.

Introduction

Tungsten carbide and the ceramic–metal composites based hard metals are extensively used, because of their unique mechanical, chemical and physical properties, as various kinds of cutting, boring and drilling tools. The influences of the composition, various additions, initial powder material characteristics, as well as the parameters of the sintering process on the mechanical properties of hard metals are well described in literature. A comprehensive review about the correlation between the microstructure and properties of WC/Co hard metals was recently published by Roebuck [1], who has shown how the size of WC grains and the Co contents influence various materials properties, such as, for example, hardness. The average grain size and the grain size distribution are the most frequently investigated microstructure parameters in hard metals, see, e.g. [2–4]. In ceramic–metal composites, the phase composition, the size and morphology of grains, the local chemical composition and/or the local composition gradients are typically the subjects of microstructural studies, see, e.g. [5–9]. The advantages and disadvantages of the experimental methods that are typically used for microstructural analysis of hard metals and ceramic–metal composites, i.e. the optical microscopy, X-ray diffraction (XRD), scanning electron microscopy (SEM) with back-scattered electrons

(BSE), scanning transmission electron microscopy (STEM) with the electron energy loss spectroscopy (EELS), secondary ion mass spectrometry (SIMS), Auger electron spectroscopy (AES) and the atom probe field ion microscopy (APFIM), were discussed in a review paper by Roebuck and Gee [10], who have shown that particularly the determination of composition gradients in materials with grain sizes below 1 μm is a difficult task. Houska [11, 12] had shown that XRD is an appropriate method for analysis of composition gradients in solids. The analysis of composition gradients using XRD exploits a very high resolution of XRD in the reciprocal space, which allows small differences in the interplanar spacings to be distinguished with a high precision. For materials in which the dependence of the interplanar spacing on the chemical composition is known, the composition gradients can be determined from the distribution of the interplanar spacings with the aid of an appropriate microstructure model, which takes into account the size and shape of individual grains. In order to create and to refine the microstructure model of the composite materials with the grain size in micrometer and sub-micrometer range, we used a combination of XRD and SEM/EBSD and SEM/EDX as suggested in [18]. The microstructure model of ceramic–metal composites describes lateral distribution of lattice parameters assuming a certain distribution of elements in hard fcc phase grains, from which the composition gradients on microscopic scale are concluded [18].

In the recent paper we focused on study of microstructural parameters of hard metals containing various fractions of WC and Ti(C,N) as hard phases and Co (and Ni) as a binder phases using the X-ray diffraction and SEM/EBSD. The EBSD analysis yielded unique information on the orientation of individual crystallites, on the grain morphology, on the grain size distribution, on the misorientation of the grain boundaries, and on the character of the grain boundaries (GBs) distributions of both, the hex-WC and the fcc-Ti(C,N) based phases individually. The XRD revealed the phase composition, microstrain, crystallite size and lattice parameters of the WC phase. Moreover, it yielded the distribution of the lattice parameters in the fcc Ti(C,N) based hard phase grains, from which the composition gradients in the hard phases were calculated using the microstructure model constructed with aid of results of the local SEM/EDX and SEM/EBSD analysis.

Sample preparation

A set of specimens containing hard WC and Ti(C,N) and soft binder (Co, Ni) phases in different proportions was prepared. The initial phase composition of powders mixtures (in mass %) is given in Table 1. The milled powders

**Table 1.** Phase composition of the initial powders.

| Sample | WC [wt%] | Ti(C,N) [wt%] | Co [wt%] | Ni [wt%] |
|--------|----------|---------------|----------|----------|
| S08 | 86 | 8 | 6 | 0 |
| S15 | 80 | 12 | 8 | 0 |
| S30 | 64 | 26 | 10 | 0 |
| S50 | 42 | 45 | 13 | 0 |
| S80 | 16 | 68 | 8 | 8 |

were mixed, pressed, de-waxed and pre-sintered. Finally, the specimens were sintered for 30 minutes at 1480°C in the nitrogen atmosphere. More details about the sample production can be found elsewhere [13].

Experimental

Since the EBSD technique is a highly surface sensitive method (the measured information comes from the depth of several tenths of nanometres) the sample surface preparation is a very critical issue. Particularly, the sample regions, which are strained and/or disturbed by the specimen cutting, have to be removed. The sample preparation procedure followed the next steps. At first, the samples were cut, then mechanically ground using silicon carbide grinding plates with decreasing roughness and polished using 6 μm , 3 μm and 1 μm diamond paste. Samples containing higher amount of the Ti(C,N) phase were finally polished using the 0.02 μm OP-AN (Struers). The EBSD investigations were performed primarily in the centre of the specimen in order to avoid the measurement of inhomogeneous parts of samples, which could occur on the samples edges.

The EBSD measurements were performed using the high-resolution scanning electron microscope LEO-1530 (Carl Zeiss) equipped with a field emission cathode and a Nordlys II EBSD detector (HKL Technology). The measurements were carried out at the acceleration voltage of 20 kV; the working distance 15 mm and the sample tilt of 70° were used. The step sizes were varied from 50 to 150 nm, depending on the materials grain size. For identification and indexing of the Kikuchi patterns as well as for the evaluation of the measured data, the software package Channel 5 (HKL Technology) was employed.

After the EBSD measurement, the polished samples were subjected to the XRD analysis. The XRD measurements were performed on conventional Bragg-Brentano URD63 diffractometer (Seifert/FPM) using the Cu K α radiation ($\lambda = 0.15418$ nm) and a graphite monochromator in the diffracted beam. The instrumental line broadening of the diffractometer was determined from the measurements on the LaB $_6$ standard from the US National Institute of Standards and Technology (NIST).

Results and Discussions

In Fig. 1, fragments of the measured X-ray diffraction patterns are shown. The positions of the peaks, corresponding to the different phases present in the samples, are schematically marked in the figure.

After the sintering process, the samples with high WC contents in the starting material (S08 - S50) contained hex-WC, fcc-binder (Co), and fcc Ti(C,N)-based hard (hereinafter referred to as hard fcc phase, only) phases. As expected, the lattice parameters of WC are for all these samples in a good agreement with the lattice parameters $a = 2.906$ Å and $c = 2.837$ Å, tabulated in [19], (record number 510939).

On the contrary, the sample S80 contains two hard fcc phases, varying in composition and therefore in lattice parameters, and the fcc binder. No peaks from the hexagonal WC are observable in the diffraction pattern. The WC was dissolved partially in the binder phase and partly in the hard fcc phase, whereas one of the hard fcc phases contains high concentration of tungsten in the grain cores, as it was confirmed by the local chemical analysis (grains with lighter shading in the cores in Fig. 2b). In hard fcc phases, pronounced changes of the peak positions and peaks shapes (asymmetry) are apparent in samples S50 and S80 (see Fig. 1). The changes are results of the diffusions and interdiffusion processes, which occurred in specimen during the sintering and/or during the powder preparation. These events are in detail described and explained in second part of the paper.

In Figs. 2 SEM/BSE micrographs of the samples containing highest amount of the WC phase (a) and highest amount of the hard fcc phases (b) are shown. The differences in the specimens' morphology are obvious. Sample S08 consists of the sharp-edged rectangular grains of WC (light gray grains) imbedded in the Co binder phase (darker regions in the micrograph) – Fig. 2a. Specimen S80, containing originally nearly 70 wt.% of the hard fcc phase, consists of spherical grains. In closer look, the pronounced core-rim structure of the grains is obvious. The core-rim structure is a consequence of the diffusion process, which occurred in individual grains during the sintering. The diffusion of elements within individual

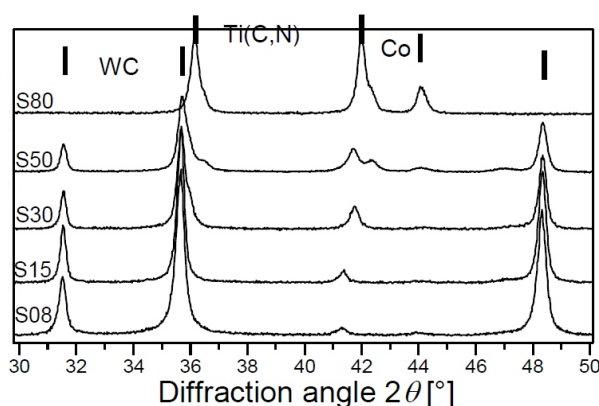


Figure 1. Fragments of measured X-ray diffraction patterns for samples under investigation. The positions of the peaks corresponding to the different phases present in the samples are schematically marked in the figure.

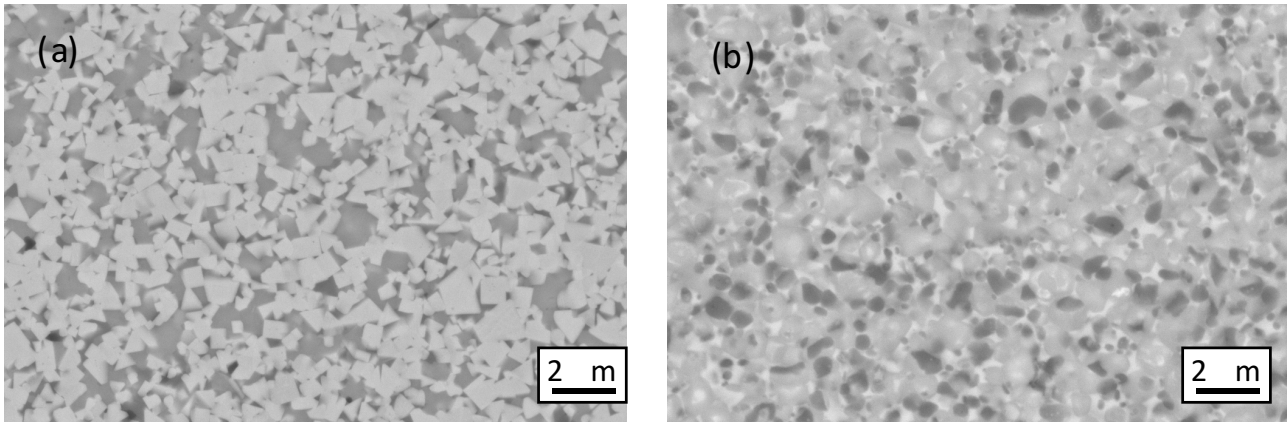


Figure 2. SEM/BSE micrographs of the sample S08 (a) and sample S80 (b) acquired at 20 kV, magnification 20000 x.

grains cause the concentration profiles gradients, which result in the lattice parameter changes and can be identified in the measured diffraction patterns as an asymmetric diffraction line broadening – see Fig. 1. The hard phase grains are again imbedded in soft binder phase (Fig. 2b). Morphology of other investigated specimens lies, depending on the WC /hard fcc phases ratio, in between of these two boundary cases. It is the combination of the sharp WC and rounded hard fcc grains imbedded in binder phase.

Volume fractions of the hard phases determined from the EBSD measurements as a function of weight fractions of given hard phases in original powder are shown in Figs. 3a,b. For both, WC and hard fcc phases, estimated volume fraction follows the linear dependence (marked in Figs. 3a,b as dashed line). However, significant deviations from the original powders compositions are obvious namely for the WC phase in sample S50, where estimated content is significantly lower and for hard fcc phases in samples S50 and S80 where the content of the fcc phases is overestimated. The reasons for these deviations are mainly caused by the difficult preparation of the sample surface for the EBSD measurements. As it was mentioned before the surface region of the specimen, where the Kikuchi pattern comes from, has to be free of deformation and strains.

However, based on the fact that the WC and hard fcc phases have different mechanical properties, for each phase a different polishing procedure leads to the best preparation of the sample surface (see details in the chapter Experimental). Diverse sample preparation for WC and hard fcc phases causes preferential removing of the minor phase, when the procedure suitable for the polishing of dominant phase is chosen. Moreover, both types of the finishing procedures adopted for polishing of the hard phases induce deformation and preferential removing of the soft and ductile binder phase. From that reason, the volume content of the binder phase was highly underestimated in all samples under study. Another effect, taking role particularly in the S80 sample, which causes disappearing of the hexagonal WC phase content, is the dissolution of the initially hex-WC grains into binder and hard fcc phases. This has in consequence increase of overall hard fcc phase amount and simultaneous disappearing of the WC phase – see Fig. 2b, where no hex-WC grains can be observed and Fig. 1, where hex-WC peaks are missing in the diffraction pattern.

The grain size distributions for the WC and fcc hard phases were determined from the measured orientation maps using the line intercept method. As a boundary be-

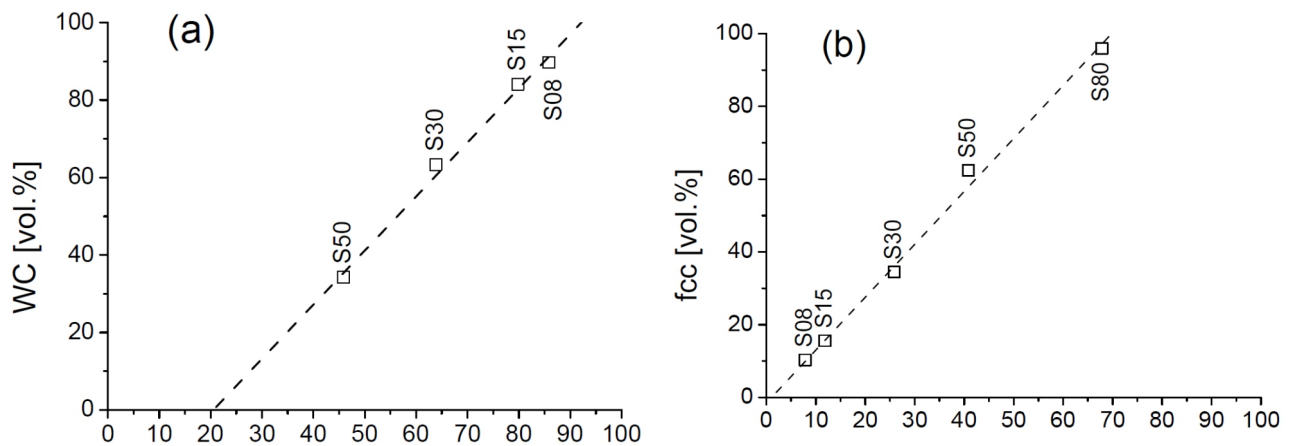


Figure 3. Volume fraction of the hard phases determined from the EBSD measurements as a function of weight fraction of given hard phase in initial powder for WC (a) and hard fcc (b) phases.

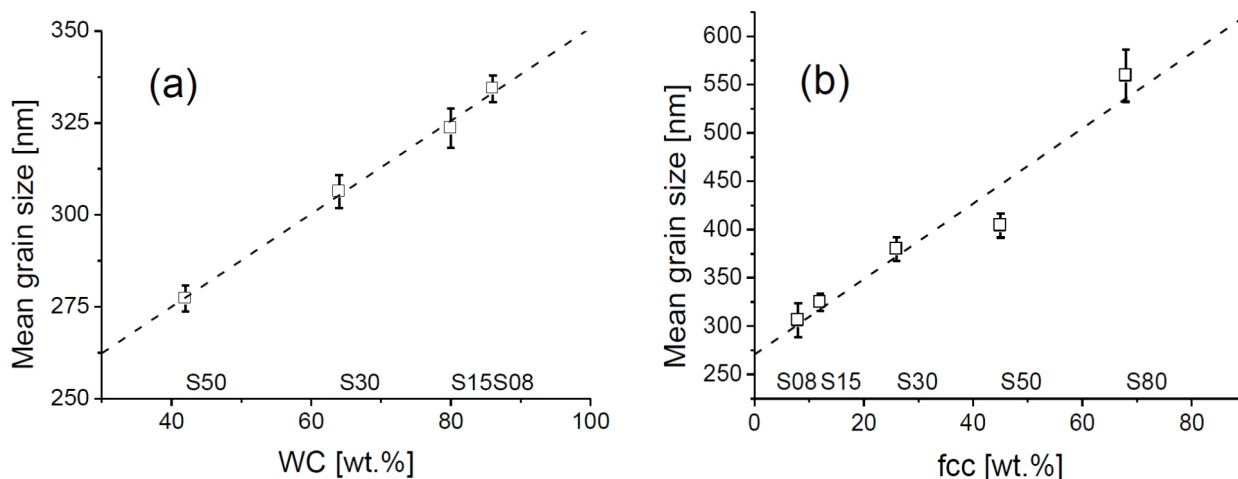


Figure 4. The mean grain size determined from the fitting of measured grain size distributions with the lognormal function as a function of initial hard phase content for hex-WC (a) and fcc (b) hard phases.

tween the different grains, the misorientation of 15° was adopted. The grain size distributions followed the lognormal distribution for all samples under study. The mean grain size, determined from the fitting of measured grain size distributions with the lognormal function, as a function of initial hard phase content is for both hard phases shown in Figs. 4a,b. The mean grain size increases from approximately 280 nm in sample S50 to approximately 330 nm in sample S08 for WC phase and simultaneously increases from 300 nm in sample S08 to roughly 550 nm in sample S80 for fcc hard phases – see Figs. 4a,b. This is rather surprising result, because in SEM micrographs the WC grains seems to be bigger than hard fcc grains (compare Figs. 2a,b). This is caused by the fact, that WC grains are not individual crystallites, but conglomerates of crystallites and vice versa core-rim structure of hard fcc grains evoking the appearance of several grains is in reality only one grain containing however the concentration profile gradient, but single similar crystal orientation. This effect can lead to significant deviations in grain size distribution determination using only the classical optical or SEM micrographs. Both of these two methods will yield overestimated value of the mean grain size for WC and underestimated value of the mean grain size for hard fcc phases. Therefore all grain size distributions determined using methods based only on the image analysis (different grains are estimated due to the variations in the micrograph colour) have to be compared with results obtained from the EBSD measurements, which is the method determining the individual grains, by definition, as a part of material having similar crystal orientation.

Orientation information obtained for each measured point of the EBSD map allows the orientation relationship between pairs of distinct points (so called misorientation) for all individual phases present in the sample to be calculated. The correlated misorientation distribution based on the calculation of the misorientations between nearest neighbour points therefore yields information on the character and the fraction of grain boundaries, while for the calculation of the uncorrelated misorientation distribution randomly chosen pairs of measured orientations are used,

which holds the information on the texture and morphology of specimen. The misorientation distributions for both hard phases in sample S30 are shown in Figs. 5a,b. The correlated misorientation distributions deviate from the random theoretical misorientation distribution [16] (solid line in Figs. 5) at low angles for both hard phases, which point out to higher amount of low angle grain boundaries (LAGBs) existing in hard phases. Moreover, we can observe significant maxima at approximately 90° in the WC phase (Fig. 5a).

From misorientation distribution, the fraction of the low angle grain boundaries (LAGBs) and high angle grain boundaries (HAGBs) can be determined. As a boundary between the LAGBs and HAGBs the angle of 15° derived by Brandon [14] was chosen. In Figures 6a,b the evolution of the LAGBs/HAGBs fractions for WC and hard fcc phases respectively, as a function of the initial hard phase amount are shown. Only results from specimens containing significant amount of investigated phases are shown in plots. For that reason, the results for hard fcc phase in sample S08, subjected to high error, are disregarded. We can observe slight linear increase of the HAGBs on the expense of LAGBs with increasing amount of initial hard phase in WC grains. There exist more than 80 % of the HAGBs in the WC hard phase, in all samples containing significant amount of WC, in all samples under study – Fig. 6a. The fraction of the HAGBs/LAGBs is, in the bounce of errors, constant in the hard fcc phases, however the ratio of HAGBs/LAGBs is approximately 55/45 % contrary to WC phase, where the amount of HAGBs was significantly higher – compare Figs. 6a and 6b.

Uncorrelated misorientation distributions tend to the theoretical random orientation distributions [16] (solid line in the misorientation distribution plots) for both WC and hard fcc phases in all samples under investigation. This is a consequence of the material morphology homogeneity (no special shapes of grains – for example elongated in one direction, were observed) and absence of the preferred orientation of crystallites – texture, which is even not expected to occur in sintered materials.

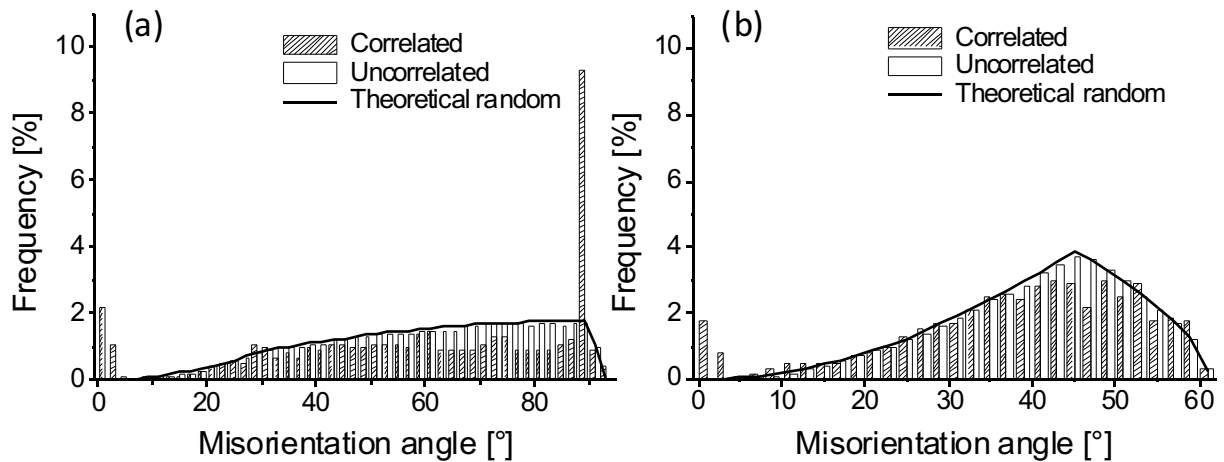


Figure 5. Correlated (hatched bars), uncorrelated (white bars), and theoretical random (solid line) distributions as function of misorientation angles in sample S30 for WC (a) and hard fcc (b) phases.

The distinct sharp maximum appearing in the correlated misorientation distribution plot of WC hard phase at misorientation angle of 90° (Fig. 5a) denotes the presence of some special HAGBs. To distinguish what type of grain boundary it is we can, for each pair of neighbour measured points, calculate the axis of misorientation and construct the angle/axis misorientation distributions (the frequencies of axes are plotted as a function of misorientation angle). In Fig. 7 angle/axis misorientation distributions for WC phase in sample S30 are shown. We can clearly identify the global maximum corresponding to the rotation of 90° around 01-10 axis. Another local maximum corresponds to the rotation of 60° around -12-10 axis. With accordance to the results published in [15] these special high angle grain boundaries correspond to the $\Sigma 2$ and $\Sigma 4$ coincidence site lattice (CSL) grain boundaries.

To quantify the fraction of $\Sigma 2$ and $\Sigma 4$ grain boundaries, we can use the coincidence site lattice theory. Brandon criterion $\theta < \theta_c^{-1/2}$ [14], where θ is the deviation from exact CSL angle, θ_c is the LAGBs / HAGBs limit, and θ_c is corresponding CSL, was adopted as a tolerance limit from

exact CSL values. The length frequencies of $\Sigma 2$ and $\Sigma 4$ grain boundaries occurring in the hard WC phase in the samples under investigation are shown in Fig. 8. In samples heaving 80 and 64 wt. % of hex-WC in the initial powder (samples S15 and S30) the total length frequency of $\Sigma 2$ grain boundaries is around 15 %, whereas in samples heaving less or more WC phase (samples S08 and S50) the length frequency is slightly lower – between 10 and 12 %. The incidence of $\Sigma 4$ grain boundaries is the result of occurrence of the $\Sigma 2$ grain boundaries. This can be demonstrated by simple geometrical consideration. They appear when three grains meet at the triple junction while two of the grain boundaries are different $\Sigma 2$ grain boundaries then third grain boundary is the $\Sigma 4$. Therefore, their amount is connected to the overall frequency of $\Sigma 2$ grain boundaries.

During the sintering processes, diffusion of working gas and/or interdiffusion of initial powder elements can occur. The diffusion and interdiffusion phenomena are often observed mainly in the ceramic–metal composites. In our study, the diffusion processes took place in specimens con-

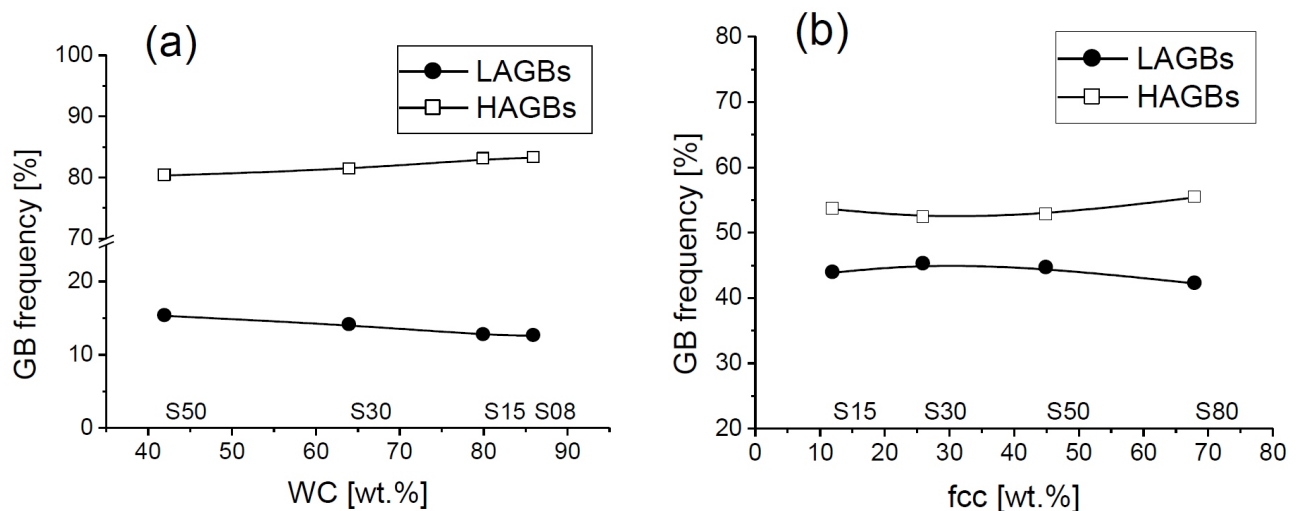


Figure 6. LAGBs and HAGBs frequency of appearance as a function of the initial amount of the hard phase for the WC (a) and hard fcc (b) phases.

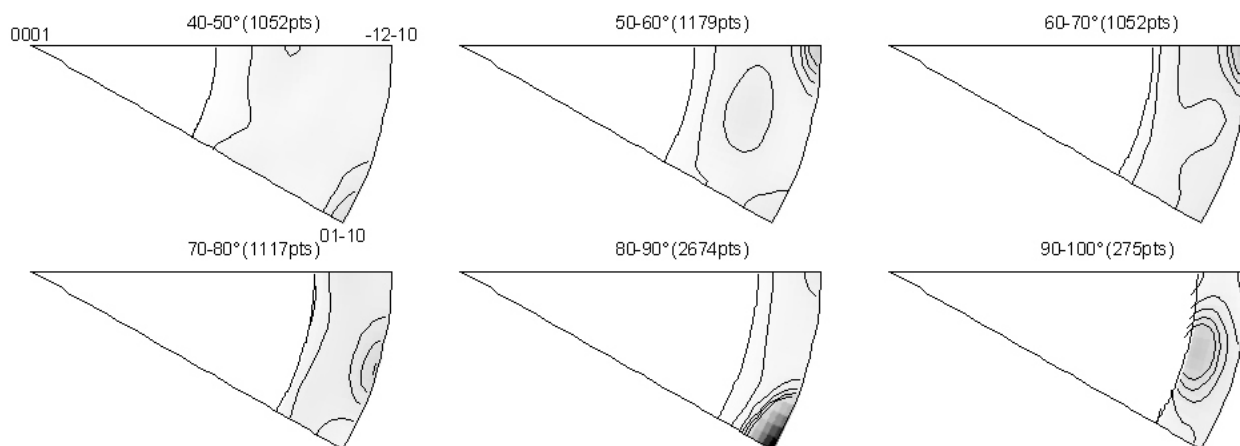


Figure 7. HAGBs distributions by axes of misorientation in WC phase. Darker colour represents higher intensity and the maximums corresponding to the $\Sigma 2$ and $\Sigma 4$ CSL, are marked in standard stereographic triangles.

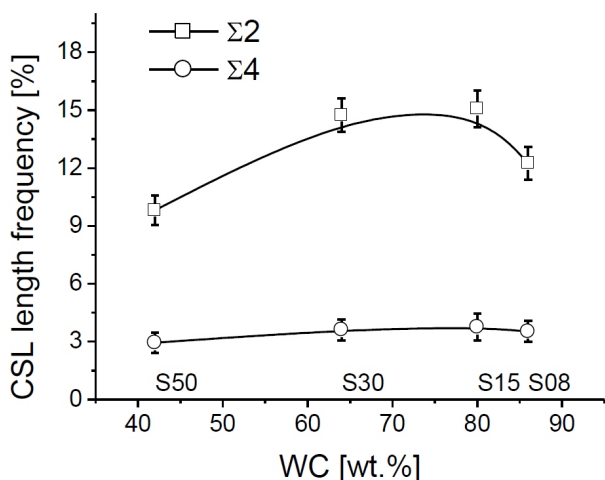


Figure 8. The evolution of total length frequency of the $\Sigma 2$ and $\Sigma 4$ CSL grain boundaries occurring in the hexagonal WC phase as a function of the initial WC hard phase fraction.

taining high amount of the fcc hard phases. As it is well seen from SEM/BSE micrographs of sample S80 (Fig. 2b) individual grains of the hard fcc phases exhibit internal structure - variations in colour correspond to the variations in composition. In the hard fcc phases the local composition gradients exist, which were caused by diffusion and interdiffusion during the sintering process. Our aim was the description of those local composition gradients, which was possible mainly in specimens containing high amount of fcc phases – S50 and S80. In remaining specimens, containing low hard fcc phase fraction, these effects were insignificant or below detection limits.

For materials in which the dependence of the interplanar spacing on the chemical composition is known, the composition gradients can be determined from the distribution of the interplanar spacings. However, the knowledge of appropriate microstructure model, which takes into account the size and the shape of individual grains and certain radial distribution of elements in hard-phase grains, is necessary. Because of high resolution of XRD in reciprocal space, the distribution of the interplanar spacing can be obtained from the X-ray line broadening with a very high pre-

cision. However, the X-ray line broadening is usually overlaid by instrumental effects. Influence of the instrumental effects on the shape of the measured XRD lines is typically expressed by the convolution of the physical function f , which is related to the microstructure of the sample, with the instrumental function g , which describes the instrumental line broadening. The measured diffraction profile h can be than written as:

$$h(x) = \int f(y)g(x - y)dy = f * g \tag{1}$$

Under assumptions of the kinematical diffraction theory, the infinitesimal diffracted intensity, scattered by the grains containing the composition gradients, observed at the diffraction angle 2θ is given by the equation:

$$\frac{dI(2\theta)}{dc} = I_0 LPA \frac{|F|^2 m}{V_e^2} \frac{dV}{dc} = K \frac{dV}{dc} \tag{2}$$

where the term dI/dc has the meaning of the intensity contribution diffracted by the infinitesimal volume of grains having the composition c , and term dV/dc the meaning of the reciprocal composition gradient in three dimensions as it is related to the infinitesimal diffracting volume. K is scaling factor containing intensity of the incident beam, Lorentz, polarization and absorption factors, multiplicity of given lattice planes, square root of the structure factor and volume of the elementary cell, whose parameters can be in the first approximation assumed constant for individual sets of lattice planes (hkl). For grains with a composition gradient, Eq. (2) describes the physical function f from Eq. (1).

In our approach we suppose linear dependence of the interplanar spacings on the concentration $d(c)=d_0+c \cdot d$, which is well fulfilled in the case of ceramic-metal composites. For calculation of the physical line broadening using Eq. (2), the following parameters of the microstructure model were used; the maximum and the minimum interplanar spacings and the steepness of the composition profile given by the square-root of the product of the diffu-

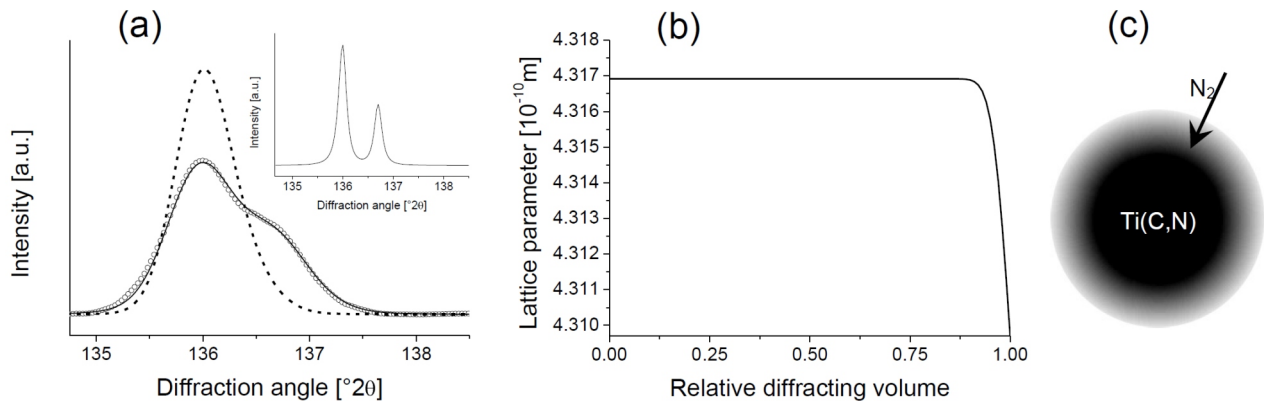


Figure 9. Diffraction lines 511/333 of the hard fcc phase measured in the sample S50. Circles show the experimental data, the solid line behind the experimental data points the re-convoluted intensities. The dashed line indicates physical profile calculated using Eq. (2) (a) from the distribution of the lattice parameters shown in (b). The inset in (a) shows the instrumental line broadening measured with the

sion coefficient and the diffusion time, (Dt), in the function $\text{erfc}(x/\sqrt{Dt})$, which approximates well the form of concentration profiles. In ceramic–metal composite materials, basically two diffusion events can occur yielding different shape of physical function f : the diffusion and the interdiffusion. The diffusion model describes diffusion processes running between diffusing species outside the grains and the individual grains themselves, whereas corresponding physical function is asymmetrical. The interdiffusion model assumes interdiffusion of elements running within individual grains, its physical function reveals two maxima.

The calculation procedure followed the next steps: first approximation of the physical function was obtained from deconvolution of the measured XRD lines [17] in order to decide whether the physical function can be approximated using a simple diffusion or interdiffusion model. In the second step, free parameters of the microstructure model were refined via fitting the calculated diffraction lines to the measured ones. The calculated diffraction profiles were obtained from the convolution of the physical function with the instrumental line broadening according to Eq. (1). The physical function was calculated using the routine described above. Instrumental broadening of diffraction lines was measured using a standard sample. More details about the calculation and fitting procedure can be found in [17, 18].

The angular distribution of the diffracted intensity in Eq. (2) is very sensitive to the composition gradient, but it is not sensitive to the position of the infinitesimal diffracting volume in the sample. This makes the determination of the position of respective diffracting volume impossible. Therefore, a complementary experimental technique is necessary to build the microstructure model, which assigns the distribution of the interplanar spacings obtained from the X-ray diffraction to the positions of the respective infinitesimal volumes within individual grains. Moreover, this microstructure model must be complemented by information about the shape and size of the grains. Information on the local chemical composition was obtained using SEM with the energy dispersive analysis of the characteris-

tic X-ray spectra (EDX). Calculated dependences of interplanar spacings (or lattice parameters) can be then, under assumptions of spherically symmetrical grains, confirmed by the SEM/EBSD measurements, with aid of known dependence of the lattice parameters on concentration, recalculated into the dependence of lattice parameter versus radial distance from the grain centre.

In sample S50 the deconvolution of the measured XRD profile corresponding to the fcc hard phase showed an asymmetric physical profile, which is the indication of diffusion process occurring during the sintering and causing variations of the lattice parameter within individual grains. Measured, physical and reconvoluted profiles of the 511/333 line, together with instrumental profile, are shown in Fig. 9a. The reflection 511/333 was chosen since it does not overlap with peaks from WC and binder phase.

The lattice parameter varies from the rim of the grains into the grain centre from 4.3097 Å to 4.3169 Å. This is a consequence of the diffusion of nitrogen during the sintering. Increasing amount of the nitrogen decreases the lattice parameter of the Ti(C,N) phase. In Fig. 9b the dependence of the lattice parameter on the relative diffracting volume is shown. The zone where the nitrogen diffused is however quite narrow. It is only about 10% of the grain radius. The diffusion process is schematically drawn in Fig. 9c, where the nitrogen richer grain rim is shown.

In sample S80 the deconvolution of the measured XRD profile has shown a physical profile containing two distinct peaks, which means that the sample consists of two hard fcc phases. The concentration profile fitting routine was modified to comprise the microstructure of two phases. Both phases were described with own set of parameters and each distribution function was approximated by a simple error function. Figure 10a shows measured, physical and reconvoluted profiles of 422 diffraction line. In Fig. 10b refined distribution functions for lattice parameters that yielded the best match between the intensities calculated using above described approach and the measured intensities in sense of the least-squares method are shown. Transformation from the relative diffracting volume to relative distance from the grain centre, which is possible because

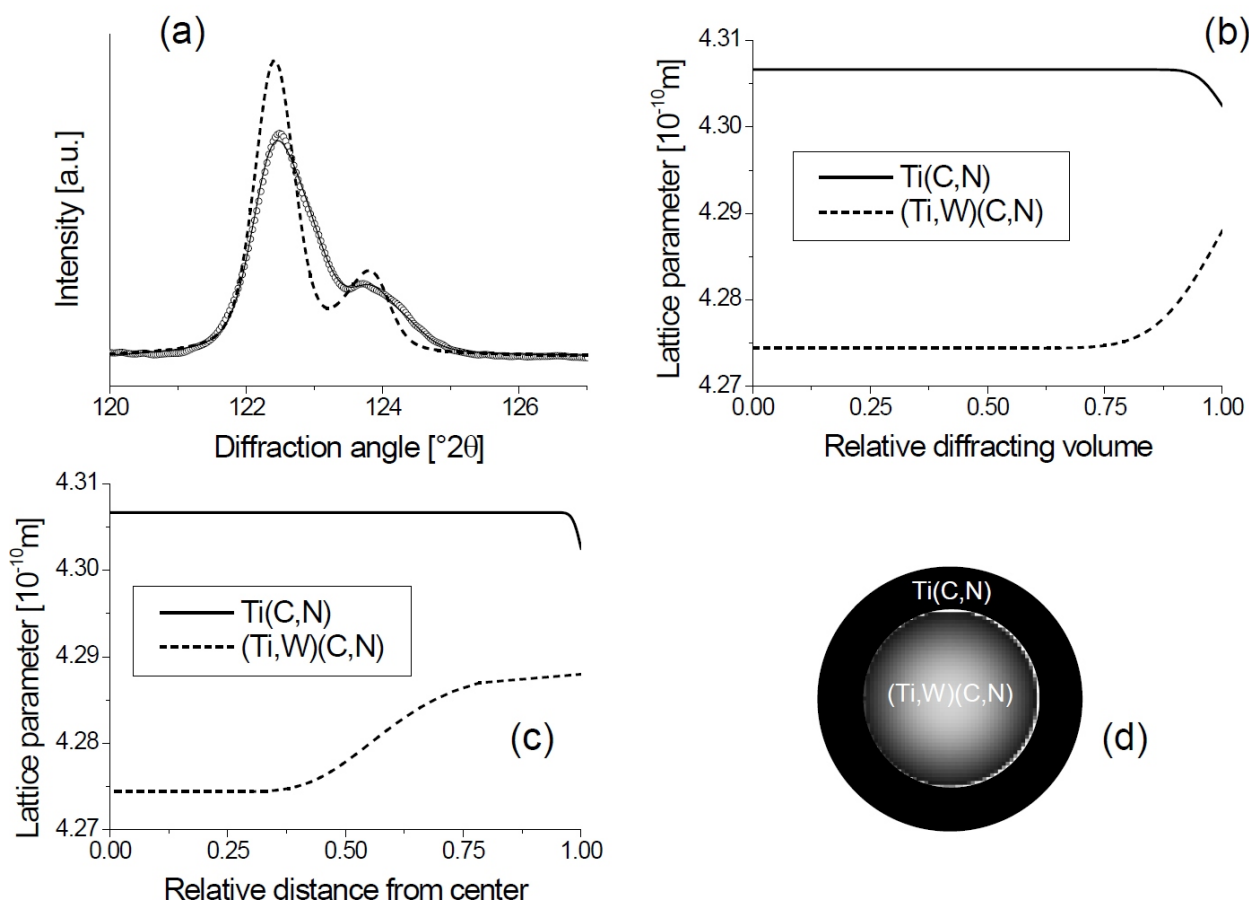


Figure 10. Diffraction lines 422 of the hard fcc phases measured in the sample S80. Circles show the experimental data, the solid line behind the experimental data points the re-convoluted intensities. The dashed line indicates physical profile calculated using Eq. (2) (a) from the distribution of the lattice parameters shown in (b). Dependence of the lattice parameter on the relative distance from the centre of idealized spherical grains (c). Schematic drawings of the second hard fcc phase - (Ti,W)(C,N) grains, having high tungsten concentration in the grain core.

the grains in sample S80 have shape that can be idealized as spherical, yield dependence shown in Fig. 10c. The upper line corresponds to original fcc hard phase, where the concentration profile and the change in the lattice parameter is cause by the diffusion of the nitrogen into grains, similarly as it was described for sample S50 (in Figs. 10 marked as Ti(C,N)). The lattice parameter varies from the rim of the grains into the grain centre from 4.3025 Å to 4.3067 Å, and analogously to the hard phase grains in the sample S50 the zone where the nitrogen diffused into the grain is quite narrow – only about 10 – 15% of the grain radius.

On the contrary, bottom line corresponds to the second hard fcc phase, marked in Figs 10 as (Ti,W)(C,N). This second hard fcc phase contains high concentration of tungsten in the grain core. The higher concentration of the tungsten in the centre of some grains observed by spatially resolved SEM/EDX analysis is clearly visible in SEM/BSE micrographs (brighter colour in the core of some grains in Fig. 2b). Tungsten occupying some atomic positions in the hard fcc phase decreases the lattice parameter (record number 201309 in [19]), which effect is visible from the bottom line in Fig. 10c. Close to the rim of the grain, the lattice pa-

rameter is higher due to lower concentration of tungsten than in the grain centre, where the tungsten concentration is high. The lattice parameter increases from the centre of the grains into the grain edge from 4.2744 Å to 4.2879 Å. The volume fraction of the second, tungsten rich, fcc phase has to be significantly lower than volume fraction of the major fcc phase, because there was initially very low content of WC in sample S80. The lower volume fraction of the second tungsten rich fcc phase corresponds to the lower integrated intensity of the physical profile function of that phase (smaller peak at higher diffraction angles in Fig. 10a).

Conclusions

A set of hard metals varying in the WC / fcc hard phases ratio was prepared. The specimens were studied using the X-ray diffraction and SEM with registration of the electron backscatter diffraction patterns (SEM/EBSD). Based on the XRD observations, we described the phase composition of materials as a function of the starting powder phase composition. The SEM/EBSD yielded information about

the grain size and grain boundary distributions in the hard phases. The mean grain size in WC and fcc hard phases increases with increasing fraction of given hard phase. This is a consequence of fact, that in material consisting dominantly of one phase, more grains of individual hard phases can be in direct contact and the grain growth can take place during the sintering. We calculated the ratio of the high and low angle grain boundaries. A high amount of 2 and 4 coincidence site lattice (CSL) grain boundaries were observed in the WC phase. No preferred orientation of crystallites was found in both hard phases. In samples containing high fraction of the fcc hard phases, the local concentration gradients were identified in the fcc hard phases grains from the asymmetry of the XRD lines. With the help of the SEM/EBSD and local chemical composition information obtained from SEM/EDX measurements, the microstructural models of hard fcc grains were created. Radial distributions of the lattice parameters in the hard fcc phases grains were calculated from the concentration profile fitting of measured XRD line profiles. In the sample with the lowest starting WC contents, WC dissolved in the binder and hard fcc phase. The formation of second hard fcc (Ti,W)(C,N) phase having high concentration of tungsten in the grain cores was observed. The combination of the spatially resolved (SEM/EBSD and SEM/EDX) with the XRD analysis yield unique complementary information about the microstructure of the hard metals.

Acknowledgments

This work was financially supported by the German Scientific Council (DFG) as part of a research project within the Collaborative Research Centre SFB 920. The authors would as well like to acknowledge the financial support through the Dr. Erich-Krüger-Stiftung, this is subproject #8 from Freiberg High-Pressure Research Centre FHP.

References

1. B. Roebuck, *Int J Refract Met Hard Mater* **24**, 101–108, (2006).
2. H. Engqvist, B. Uhrenius, *Int J Refract Met Hard Mater* **21**, 31–35, (2003).
3. V.T. Golovchan, N.V. Litoshenko, *Int J Refract Met Hard Mater* **21**, 241–244, (2003).
4. V. Kumar, Z.Z. Fang, S.I. Wright, M.M. Nowell, *Metal Mater Trans A* **37**, 599–607, (2006).
5. L. Chen, W. Lengauer, K. Dreyer, *Int J Refract Met Hard Mater* **18**, 153–161, (2000).
6. H.O. Andrén, *Mater Design* **22**, 491–498, (2001).
7. B. Wollein, M. Bohn, W. Lengauer, *Surf Interface Anal* **34**, 343–345, (2002).
8. W. Lengauer, *Mat-wiss Werkstofftech* **36**, 460–466, (2005).
9. G. Östberg, H.O. Andrén, *Metal Mater Trans A* **37**, 1495–1506, (2006).
10. B. Roebuck, M.G. Gee, *Proceedings of the 12th international Plansee seminar*, vol. 2, H. Bildstein, H.M. Ortner Eds., Reutte/Tirol, pp. 1–29, (1989).
11. C.R. Houska, *J Appl Phys* **41**, 69–75, (1970).
12. D.R. Tenney, J.A. Carpenter, C.R. Houska, *J Appl Phys* **41**, 4485–4492, (1970).
13. D.S. Janisch, W. Lengauer, K. Rödiger, K. Dreyer, H. van den Berg, these proceedings.
14. D. G. Brandon, *Acta Metallurgica* Vol. **14**, 1479, (1966).
15. S. Lay and M. Loubradou, *Phil. Mag.* Vol. **83**, No. 23, 2669–2679, (2003).
16. J. K. Mackenzie, *Acta Metallurgica* Vol. **12**, 223, (1964).
17. D. Rafaja, *Mater Struct* **7**, 43–50, (2000).
18. D. Rafaja, M. Dopita, M. Masimov, V. Klemm, N. Wendt, W. Lengauer, *Int J Refract Met Hard Mater* **26**, 263–275, (2008).
19. Powder Diffraction File PDF-2 on CD-ROM. Philadelphia: International Centre for Diffraction Data; (2003).